ELSEVIER

Journal of Fluids and Structures 23 (2007) 959–982

JOURNAL OF FLUIDS AND STRUCTURES

www.elsevier.com/locate/jfs

Dynamic stall model for wind turbine airfoils

J.W. Larsen[a,*], S.R.K. Nielsen[a], S. Krenk[b]

[a]*Department of Civil Engineering, Aalborg University, DK-9000 Aalborg, Denmark*
[b]*Department of Mechanical Engineering, Technical University of Denmark, DK-2800 Lyngby, Denmark*

Received 4 April 2006; accepted 18 February 2007
Available online 11 May 2007

Abstract

A model is presented for aerodynamic lift of wind turbine profiles under dynamic stall. The model combines memory delay effects under attached flow with reduced lift due to flow separation under dynamic stall conditions. The model is based on a backbone curve in the form of the static lift as a function of the angle of attack. The static lift is described by two parameters, the lift at fully attached flow and the degree of attachment. A relationship between these parameters and the static lift is available from a thin plate approximation. Assuming the parameters to be known during static conditions, nonstationary effects are included by three mechanisms: a delay of the lift coefficient of fully attached flow via a second-order filter, a delay of the development of separation represented via a first-order filter, and a lift contribution due to leading edge separation also represented via a first-order filter. The latter is likely to occur during active pitch control of vibrations. It is shown that all included effects can be important when considering wind turbine blades. The proposed model is validated against test data from two load cases, one at fully attached flow conditions and one during dynamic stall conditions. The proposed model is compared with five other dynamic stall models including, among others, the Beddoes–Leishman model and the ONERA model. It is demonstrated that the proposed model performs equally well or even better than more complicated models and that the included nonstationary effects are essential for obtaining satisfactory results. Finally, the influence of camber and thickness distribution on the backbone curve are analysed. It is shown that both of these effects are adequately accounted for via the static input data.

Keywords: Dynamic stall; Wind turbines; Wing sections; Airfoil flow

1. Introduction

Wind turbines are designed with increasingly slender blades and blade controls that can react rapidly to changing loading conditions. Thus, it becomes increasingly important to account for nonstationary load effects. The basic nonstationary mechanisms are illustrated in Fig. 1, showing a typical airfoil profile with relative flow velocity V, angle of attack α, and lift force L per unit length. The lift force is represented via the nondimensional lift coefficient c_L, defined by

$$L = c_L \tfrac{1}{2}\rho V^2 c, \tag{1}$$

*Corresponding author. Tel.: +45 9635 7230; fax: +45 9814 2555.
E-mail address: i5jwl@civil.aau.dk (J.W. Larsen).

0889-9746/$ - see front matter © 2007 Elsevier Ltd. All rights reserved.
doi:10.1016/j.jfluidstructs.2007.02.005

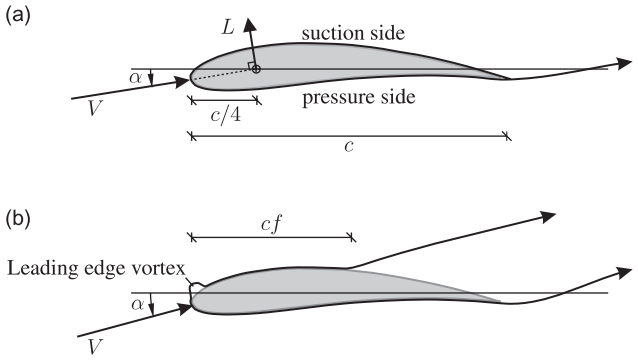

Fig. 1. Principles of attached and separated flow.

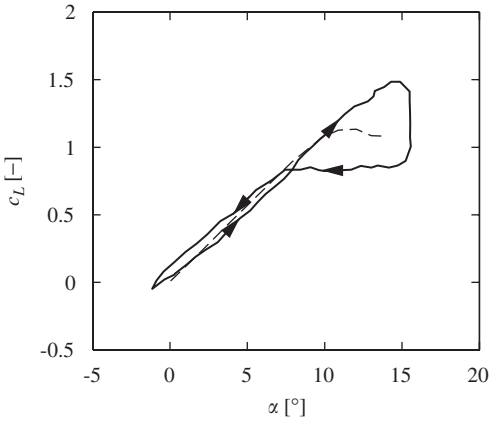

Fig. 2. Lift coefficient under static and dynamic stall situations: ––, static lift; —, dynamic lift (Leishman, 2000, p. 385).

where c is the chord length. It is well established that under stationary attached flow conditions the lift force L acts approximately in the forward quarter-point, named the aerodynamic centre, and is approximately a linear function of the angle of attack α, when α is sufficiently small (Bisplinghoff, 1996).

At a limiting value of the angle of attack α_s the flow pattern changes, and the lift force passes through a maximum. This is the phenomenon of static stall. A typical curve of the static lift coefficient c_L is shown as the dashed line in Fig. 2. Stall is associated with separation of the flow at the suction side of the profile as illustrated in Fig. 1(b). The degree of separation can be represented in an approximate way by the distance cf from the leading edge to the separation point, where the nondimensional parameter f is a measure of the degree of separation. For fully attached flow $f = 1$, and for separated flow f decreases towards zero with increasing separation.

Under nonstationary conditions, it takes some time for the flow to approach the stationary flow pattern. For fully attached flow, analytic solutions can be obtained for harmonic motion of the airfoil as well as for a step function change in position (Fung, 1993, pp. 206). In principle, these solutions involve translation as well as rotation of the airfoil, but for the present purpose it is sufficient to combine the effect of the motion into an effective angle of attack. This is described in Section 4. The analytical solutions indicate delayed lift during fully attached conditions with a lower lift at increasing α and higher lift at decreasing α compared to the quasi-static solution. This effect is also seen on the dynamic lift in Fig. 2 at low angles of attack. When the flow is separated during the motion, the degree of attachment, represented by the parameter f, also exhibits delay with respect to its stationary value. The delay in the flow and the degree of separation for harmonic motion influences the stall phenomenon. A typical dynamic stall curve is plotted as the full line in Fig. 2. It is seen that for a harmonic variation of the angle of attack α between 0° and 15°, the occurrence of stall is delayed, and the lift during the phase of decreasing α is considerably lower than during the increasing phase. Thus, dynamic stall typically involves an increased range of attached flow and different branches for increasing and decreasing angle of attack.

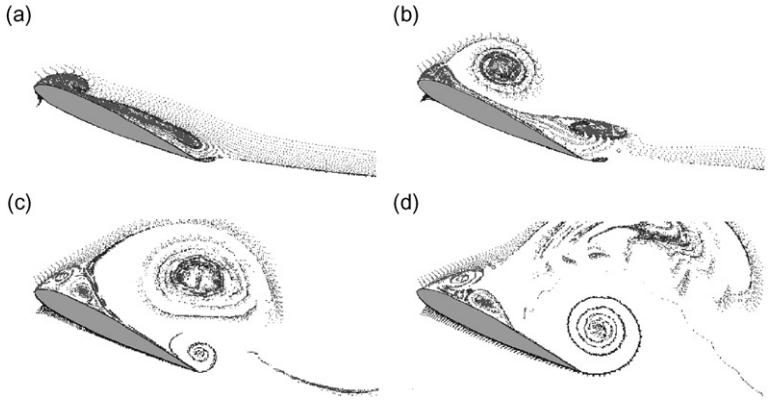

Fig. 3. Flow visualisation of a CFD calculation performed on a NACA-0015 wing section during dynamic stall conditions. (a) Leading edge separation starts. (b) Vortex build-up at the leading edge. (c) Detachment of leading edge vortex and build-up of trailing edge vortex. (d) Detachment of trailing edge vortex and breakdown of leading edge vortex (VISCWIND, 1999).

In addition to trailing edge separation, a separation bubble may develop in the boundary layer at the suction side of the profile close to the leading edge, a phenomenon characteristic for thin profiles. In front of the bubble the boundary layer is attached, whereas behind the bubble two situations can occur. In one case, the boundary layer downstream of the bubble is turbulent, enhancing the tendency of attachment. This situation is illustrated in Fig. 1(b). In the other case, the boundary layer detaches fully, creating separation from the leading to the trailing edge. Under quasi-static conditions, the situation is very unstable, and in fact both situations can occur at the same angle of attack. Hence, two different lift curves can occur (Bak et al., 1999). This phenomenon is called double stall. Under dynamic oscillations, the flow will separate immediately at the separation bubble. Even though the flow is fully separated over the profile, experimental data show an almost linearly increasing lift force (Leishman, 2000). This increase in lift is generated by a rising pressure peak at the leading edge and a large vortex created in the turbulent wake as the trailing edge separation point moves abruptly to the leading edge. At low pitch velocities, leading edge separation is usually no problem, but in recent years a wish for active control of tower and blade vibrations has led to pitch control of large wind turbine wings with pitch velocities of up to $20^\circ/s$. Also, large deformations due to flexible wings may produce high amplitude changes in the angle of attack. Under such conditions, leading edge separation may contribute significantly to the lift. As the angle of attack is increased, the vortex builds up in strength and finally detaches from the leading edge travelling downstream. CFD calculations indicate the creation of a secondary vortex with opposite circulatory contribution at the trailing edge during dynamic stall conditions. The trailing edge vortex builds up during dynamic stall, and at some point it detaches and convects downstream similar to the leading edge vortex. A CFD calculation of a NACA-0015 profile in dynamic stall conditions is illustrated in Fig. 3. The dynamic stall calculation has been performed by Risø National Laboratory, Wind Energy and Atmospheric Physics Department within the EC project VISCWIND (VISCWIND, 1999). The dots indicate particles added to illustrate the flow characteristics. Fig. 3(a) illustrates the onset of leading edge separation with the entire boundary layer starting to detach. Fig. 3(b) shows the build-up of the leading edge vortex, which in Fig. 3(c) detaches and moves downstream, while a trailing edge vortex starts building up. Finally, Fig. 3(d) shows the detachment of the trailing edge vortex and breakdown of the leading edge travelling vortex. Both experimental data and CFD calculations indicate that the flow changes, caused by the leading edge separation vortex, generate an increased suction contribution, leading to an increased lift even after flow separation has occurred. This effect may be seen in Fig. 2 as the dynamic curve that continues to increase above the static stall angle.

At low-frequency changes of the angle of attack, flow situations including trailing edge separation occur at increasing angle of attack, where the flow separation point moves from the trailing to the leading edge. At decreasing angle of attack, the separation point moves back from the leading to the trailing edge. Both situations are described by the movement of the trailing edge separation point. As the frequency increases, leading edge separation conditions are likely to happen as illustrated in Fig. 3, especially for thin profiles. Under these conditions, no distinct position of the trailing edge separation point can be followed and separation over the entire profile occurs more or less instantaneously at increasing angle of attack. Flow reattachment at decreasing angle of attack mainly happens with the separation point moving from the leading to the trailing edge, as was the case for low-frequency oscillations.

In summary, delay of lift during fully attached conditions and the motion of the separation point as well as leading edge separation and the dynamic interaction between leading and trailing edge vortices are constituent properties of a

load model for which dynamic stall phenomena occur. A good model of dynamic stall should describe these phenomena for different frequencies and different amplitude ranges.

There exists a great variety of dynamic stall models in the literature. These models may be categorised into three main groups:

(1) The effects of the different flow conditions described above are modelled, e.g. lift reduction due to separation, time delay effects from leading edge separation etc.
(2) The characteristics of the lift curve are modelled without resort to the generating physical mechanisms, e.g. a linear growing curve at low angles of attack, a drop in lift at a given stall angle etc.
(3) A modification of the angle of attack is made introducing a so-called dynamic angle of attack.

In a series of papers (Leishman and Beddoes, 1986a, b; Leishman, 1988), Beddoes and Leishman have developed a model for dynamic stall combining the flow delay effects of attached flow with an approximate representation of the development and effect of separation. This model was developed with helicopter rotor dynamics in mind and therefore includes a fairly elaborate representation of the nonstationary attached flow depending on the Mach number and a rather complex structure of the equations representing the time delays. In contrast, a model proposed by Øye (1991) omits the transient effects of the attached flow, and represents the dynamic stall by introducing a first-order filter on a static equivalent degree of attachment, obtained by a simple interpolation relation. Hansen et al. (2004) developed a reduced version of the Beddoes–Leishman model at Risø National Laboratories, Denmark, omitting the effects of compressible flow and leading edge separation. They introduced an interpolation relation similar to the one used by Øye to make the model valid in the entire range of the angle of attack. The Beddoes–Leishman model, Øye and Risø models may be categorised into the first group of models aiming to model the effects of the flow conditions. The so-called ONERA model by Tran and Petot (1981) is an example of the second category of modelling. In this case, the load coefficients are described by a third-order differential equation. The differential equation is split into a linear domain at low angles of attack determined by a first-order differential equation, and a stall domain determined by a second-order differential equation. Tarzanin (1972) developed a model also named the Boeing–Vertol model, based on a relation between the dynamic stall angle and static stall angle determined by Gross and Harris (1969). From this relationship a dynamic angle of attack is determined and the load coefficients are interpolated from the static data. Obviously, this final model falls into the third category of modelling approaches.

In recent years, Navier–Stokes solvers have also been used to determine airfoil loads in dynamic stall situations. Due to the extensive cost of these calculations, practical applications do not seem possible in the near future, but solving the Navier–Stokes equations gives insight into the flow and pressure changes occurring during a dynamic stall cycle. Srinivasan et al. (1995) used a Navier–Stokes solver to evaluate a variety of turbulence models. Du and Selig (1998, 2000) studied 3-D effects on the boundary layer flow of a rotating wind turbine blade by solving the steady boundary layer equations. They found that the separation is slightly postponed due to rotation of the wing, which induces an increase in lift. They suggested a modification of the 2-D static data to incorporate the rotational 3-D effects. Akbari and Price (2003) studied the effects of several parameters including reduced frequency, mean angle of attack, location of the pitch axis and the Reynolds number. They found that the Reynolds number and position of the pitch axis have little effect on the characteristics of the lift cycle, however the position of pitch axis has a major effect on the pitching moment. Wernert et al. (1996) used Particle Image Velocimetry (PIV) and Laser Sheet Visualisation to validate a numerical code based on Navier–Stokes equations. They found that the numerical and experimental results agreed, but some discrepancies were observed. A completely different approach is suggested by Suresh et al. (2003) using neural network for identifying nonlinear unsteady lift. Comparing with experimental data, they show a good agreement with their numerical model. They also argue that the proposed method is easily implemented in available codes and should be less computationally expensive than the ONERA model.

It should be noted that larger discrepancies between numerical and experimental results seem to be accepted within the so-called semi-empirical models described above than for the Navier–Stokes solvers. The goals of the semi-empirical models are not to capture every variation in the load, but to model the main characteristics in a fast and efficient way. The main drawback of the semi-empirical models is that all of them are dependent on available static data and use interpolation into tabulated values or curve fitting techniques to determine quasi-static lift values. A semi-empirical model should be able to reproduce these static values for quasi-static rates of the angle of attack, i.e. $\dot{\alpha} \simeq 0$.

In this paper, a semi-empirical dynamic stall model for the lift is formulated. The model is developed mainly with concern for realistic wind turbine flows, hence compressibility effects are omitted. An essential part is that the model should fit into the first category of semi-empirical models, hence the lift contributions introduced in the model should be explained by certain changes in flow and resulting changes in pressure. The model should be applicable both at high

pitch rates during e.g. active control or large gusts, and during normal operation conditions with low pitch rates. The proposed model introduces an analytical solution to the static lift curve in terms of lift at separated flow conditions for known position of the trailing edge separation point, (Krenk, 2006; Thwaites, 1960). This relation serves as a backbone curve for the model, when the position of the trailing edge separation point is assumed to be known for all angles of attack. These curves may be found from static experimental data. The various dynamic effects included in the model are introduced as delay terms in the parameters of the backbone function. The model combines a simple two-term memory kernel for the transient behaviour of the attached flow with a lift reduction due to separation, represented via a first-order filter, giving two state parameters to describe the flow delay under full attachment and one-state parameter to describe the delayed placement of the separation point. The reason for using two timescales under attached flow conditions is to model with sufficient accuracy both high pitch frequencies occurring e.g. during active control or normal operating conditions. Furthermore, an additional first-order filter is used to model the increased lift under leading edge separation. The advantage of this compromise is that within a fairly simple model the transients of the flow are included in a manner that is sufficiently accurate for wind turbines, and the dynamic effect of trailing edge separation in essence only introduces one additional timescale.

The numerical algorithms for the Beddoes–Leishman, Øye, Risø, ONERA and Boeing–Vertol models are described briefly in the Appendix. These models also use the approach of introducing the static lift curve as a backbone curve. The Beddoes–Leishman and the Risø models use the unsteady thin plate approximation adopted in the proposed model. Numerical simulations are made and the performance of the various models are studied and compared with existing experimental data. In the above-mentioned analyses, the profile is assumed to be a thin plate. The effect of camber and thickness under separated quasi-static flow conditions has recently been derived in closed form (Krenk, 2006) and can be included directly in the format of the present model.

2. A dynamic stall model for wind turbines

2.1. Stationary lift and separation

An essential part of a nonlinear load model is the lift reduction due to separation. The lift coefficient of the profile under fully attached flow is denoted c_{L0} and is often linearised for small α in the following manner:

$$c_{L0} = \left.\frac{\partial c_L}{\partial \alpha}\right|_{\alpha_0} (\alpha - \alpha_0), \tag{2}$$

where α_0 is the angle of attack at zero lift. For a thin plate the coefficient $\partial c_L/\partial\alpha = 2\pi$, whereas the coefficient is somewhat different for a real profile. The lift coefficient c_L under separated flow can be found from Kirchhoff flow theory using complex mapping, (Thwaites, 1960, p. 170), or more directly by a singular integral formulation of linearised airfoil flow theory (Krenk, 2006) as

$$c_L \simeq \left(\frac{1+\sqrt{f}}{2}\right)^2 c_{L0}. \tag{3}$$

According to Eq. (3), the total static lift coefficient is determined as a reduction of the linear lift according to the attachment degree f. At fully attached flow, where $f = 1$, c_L follows c_{L0}. As α increases, the separation point moves towards the leading edge and f decreases. When the separation point reaches the leading edge, $f = 0$ and $c_L \simeq \frac{1}{4}c_{L0}$ according to Eq. (3). A further increase in α will not change the location of the separation point, hence $f = 0$, but c_{L0} given by Eq. (2) increases linearly with α. As a consequence, Eq. (3) predicts a linear increase with α of $c_L \simeq \frac{1}{4}c_{L0}$ for fully separated flow. This is illustrated in Fig. 4(a) where full separation occurs at approximately 30° and the (×) symbols indicate measured lift coefficients from a NACA 63-418 profile (Abbott and von Doenhoff, 1959). According to measured values, c_L remains constant or even decreases with increasing α in this regime. To remedy this inconsistency, a modification is needed. Here the correction will be made on c_{L0}, which for $f > 0$ is determined as the linearised lift coefficient given in Eq. (2), and for $f = 0$ is set to $4c_L$. Hence, c_{L0} is determined as

$$c_{L0} = \begin{cases} \left.\dfrac{\partial c_L}{\partial \alpha}\right|_{\alpha_0} (\alpha - \alpha_0), & f > 0, \\ 4c_L, & f = 0 \end{cases} \tag{4}$$

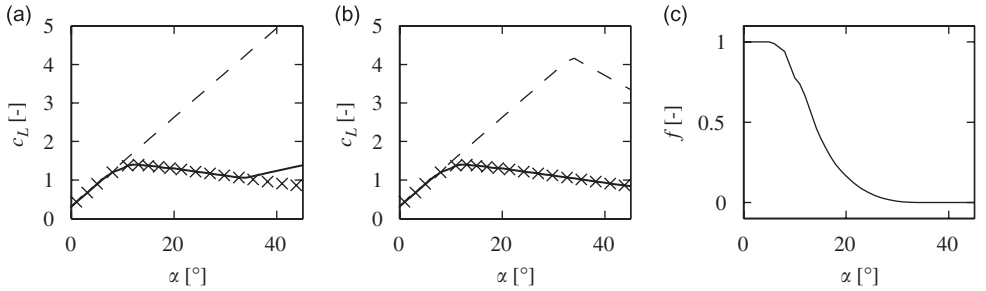

Fig. 4. Static coefficients; ×, measured values of c_L from a NACA 63-418 profile (Abbott and von Doenhoff, 1959). (a) ––, c_{L0} determined from Eq. (2); —, c_L modelled by Eq. (3). (b) ––, c_{L0} determined from Eq. (4); —, c_L modelled by Eq. (3). (c) —, f.

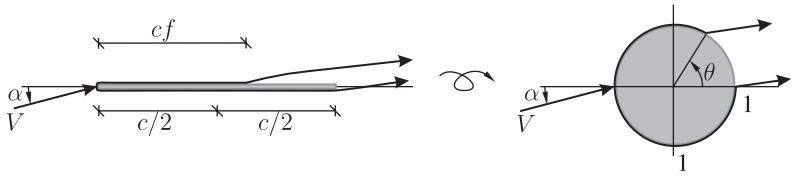

Fig. 5. Transformation into the complex plane.

and f is found from Eq. (3). This modification of c_{L0} allows the use of Eq. (3) in the entire range of α. Fig. 4(b) illustrates that by use of Eqs. (3) and (4), it is possible to reproduce the measured c_L also when full separation occurs.

The motion of the separation point may be modelled in the physical plane as done in the Beddoes–Leishman model, the Risø model and the Øye model. However, as follows from Eq. (3) changes of the lift coefficient are related to changes of the attachment degree as

$$dc_L = \frac{1}{4}\left(1 + \frac{1}{\sqrt{f}}\right) c_{L0}\, df. \tag{5}$$

Hence, at fully separated conditions ($f \simeq 0$), an increment of the degree of separation results in a large increment of the lift coefficient. In order to circumvent this singularity, the physical profile is mapped on a unit circle as traditionally performed in airfoil theory, see Fig. 5, where the idea is to use the angle θ indicating the separation point in the complex map, rather than f. The functional relationship transforming f into θ is given by

$$2f = 1 + \cos\theta, \tag{6}$$

which inserted in Eq. (3) gives

$$c_L = \cos^4(\tfrac{1}{4}\theta) c_{L0}. \tag{7}$$

This formulation removes the square root singularity around $f = 0$, corresponding to $\theta = \pi$. $\theta(\alpha)$ is found from the inverse relation of Eq. (7). Hence, in the numerical algorithm, a set of measured lift data $c_L(\alpha)$ is needed to determine the separation parameter $\theta(\alpha)$.

The moment M may be represented by the nondimensional moment coefficient in the following manner:

$$M = c_M \tfrac{1}{2}\rho V^2 c^2, \tag{8}$$

where M is measured in the clockwise direction around the centre. Assuming the position of the separation point to be known from Eq. (3) and measured value of c_L, Krenk (2006) derived the following expression for the static moment coefficient for a thin plate profile:

$$c_M = \frac{1}{4}\left(\frac{1+\sqrt{f}}{2}\right)^2 \left[1 - \frac{1}{4}(1 - 6\sqrt{f} + 5f)\right] c_{L0}. \tag{9}$$

The moment coefficient is given in terms of the attachment degree and at fully attached flow conditions $c_M = \frac{1}{4} c_{L0}$, which identifies the location of the aeroelastic centre at the quarter chord point. Both the Beddoes–Leishman model and Risø models use an empirical relation for determining the movement of the centre of pressure given as c_M/c_L in terms of

the static attachment degree, i.e. the moment coefficient is determined from the static lift and the location of the centre of pressure.

2.2. Dynamic lift and separation

So far, only stationary conditions have been considered. In this section, the nonstationary lift is modelled due to time dependent flow changes. Two main flow situations are considered. One is at low angles of attack with fully attached flow, where the flow adjusts so that the separation point is located at the trailing edge, and a situation with separated flow where the movement of the trailing edge separation point is delayed compared to the quasi-static movement.

First consider the fully attached flow situation. For a change $\mathrm{d}\alpha$ in the angle of attack, a small separation occurs before the separation point is reestablished at the trailing edge by circulation built-up around the profile. This change in circulation creates a corresponding change in lift. Hence, the increment $\mathrm{d}c_{L0}$ of the linear lift due to an increment $\mathrm{d}\alpha$ of the angle of attack is not achieved instantaneously. Given the linearised conditions (2), this delay can be modelled via the introduction of an impulse response function $\Phi(t)$, so the increment $\mathrm{d}c_{L0,d}(t)$ at time t due to an increment $\mathrm{d}\alpha(\tau)$ at an earlier time τ can be written

$$\mathrm{d}c_{L0,d} = \Phi(t-\tau)\mathrm{d}c_{L0}(\tau). \tag{10}$$

In Eq. (10) and below, the dynamic lift is indicated by the subscript d. The impulse response function fulfills $\Phi(\infty) = 1$. For incompressible flow, it can be shown for a thin profile that half the increment is felt instantaneously, so $\Phi(0) = \frac{1}{2}$, see (Fung, 1993, pp. 206). Upon superposition of the effects of all previous increments, the linear dynamic lift, valid for attached flow conditions, is given as

$$c_{L0,d}(t) = \int_{-\infty}^{t} \Phi(t-\tau)\dot{c}_{L0}(\tau)\,\mathrm{d}\tau. \tag{11}$$

The approach chosen here for the linear lift coefficient is similar to that of the Beddoes–Leishman model, described in Appendix A.1. However, the compressibility terms are neglected. The analytical solution of $\Phi(t)$ may be approximated by a first-order filter with a single timescale with the initial condition $\Phi(0) = \frac{1}{2}$ and the limit $\Phi(\infty) = 1$, but as mentioned earlier, both high- and low-frequency components need to be modelled accurately, hence two timescales are needed. In what follows, it is assumed that $\Phi(t)$ may be approximated with the expression

$$\Phi(t) = 1 - A_1 \mathrm{e}^{-\omega_1 t} - A_2 \mathrm{e}^{-\omega_2 t}, \tag{12}$$

where A_1, A_2, ω_1 and ω_2 are profile dependent variables describing the time delay. For a thin profile in incompressible flow, $A_1 + A_2 \simeq \frac{1}{2}$ (Fung, 1993), and ω_1 and ω_2 represent the timescale for low- and high-frequency contributions, respectively. Then a differential description of the convolution integral (11) can be obtained as follows. Let $c_1(t)$ and $c_2(t)$ be state variables related to the filter, defined by the first-order differential equations

$$\dot{c}_j(t) + \omega_j c_j(t) = A_j \dot{c}_{L0}(t), \quad j = 1, 2. \tag{13}$$

Then, $c_{L0,d}(t)$ can be represented by the following output equation:

$$c_{L0,d}(t) = c_{L0}(\alpha) - c_1(t) - c_2(t). \tag{14}$$

Next consider a situation under separated flow conditions. According to Eq. (7), a step change in α is felt instantaneously through a direct change in θ. In a real flow situation, a time interval is observed during which the separation angle moves to the new stationary value. Due to this delay, the attachment angle is lower at increasing α and larger at decreasing α than the corresponding stationary value giving larger and lower lift forces, respectively.

Expression (14) only includes the circulatory flow lift. At large pitch rates, noncirculatory effects may contribute significantly. The Beddoes–Leishman model (Leishman, 1988, 2000; Leishman and Beddoes, 1986a, b; Beddoes, 1978) introduces extra state variables to account for the dynamics of the noncirculatory effects. However, when considering wind turbine dynamics at relatively low flow velocities, it is sufficient to include the noncirculatory effects as an added mass contribution adding an extra term $\pi c\dot{\alpha}/2V$ to $c_{L0,d}$, (Hansen et al., 2004). No additional state variables or calibration parameters are introduced via this contribution, hence the complexity and computational cost have not increased significantly.

Due to the relation between changes in separation and lift given in Eq. (5), the nonstationary effect on c_L from the delayed separation is modelled as a delay on the separation variable. The delayed motion of the separation point and hence the separation angle under dynamic conditions is described via a dynamic attachment angle θ_d obtained as the

solution to the first-order differential equation

$$\dot{\theta}_d(t) = -\omega_3(\theta_d(t) - \theta(\alpha)). \tag{15}$$

A similar approach has been used in the Beddoes–Leishman model, the Risø model and the Øye model, where a dynamic attachment degree f_d is used, obtained from the differential equation

$$\dot{f}_d(t) = -\omega_3(f_d(t) - f(\alpha)). \tag{16}$$

Although only valid for static conditions, the reduction of the dynamic linear lift coefficient $c_{L0,d}(t)$ due to the dynamic attachment angle is again calculated via Eq. (7) as follows:

$$c_{L,d}(t) = \cos^4(\tfrac{1}{4}\theta_d)c_{L0,d}(t). \tag{17}$$

2.3. Leading edge separation

As mentioned earlier, experimental data indicates that leading edge separation generates a linear increasing lift curve even at full separation due to a pressure peak forming at the leading edge and a large vortex forming in the wake of the profile at increasing α. Instead of modelling these contributions separately, a combined lift correction is added to $c_{L,d}(t)$ to create this linear lift curve. This is possible because the total lift is assumed to follow the linear curve $c_{L0,d}(t)$ as long as the vortex is found on the profile. Assuming this, the additional lift contribution $\Delta c_L(t)$ becomes

$$\Delta c_L(t) = c_{L0,d}(t) - c_{L,d}(t). \tag{18}$$

At a certain angle α_v, the leading edge vortex detaches from the leading edge and travels downstream over the profile with the velocity $\frac{1}{3}V$, (Green et al., 1992; Beddoes, 1978). Green et al. (1992) came to approximately the same vortex convection velocity for a variety of profiles, hence showing that the vortex travelling velocity is independent of profile shape. The travelling vortex keeps building up strength as long as it is located somewhere on the profile. As it reaches the trailing edge, the vortex contribution stops building up corresponding to $\Delta\dot{c}_L(t) = 0$, and the vortex with opposite circulation starts to develop at the trailing edge, see Fig. 3. The trailing edge vortex counteracts the leading edge travelling vortex and the lift starts diminishing. This diminishing effect is assumed to be described by the following first-order differential equation:

$$\dot{c}_{L,v}(t) + \omega_4 c_{L,v}(t) = \begin{cases} \Delta\dot{c}_L(t) & \text{for } \alpha > \alpha_v \text{ and } \dot{\alpha} > 0, \\ 0 & \text{otherwise,} \end{cases} \tag{19}$$

where $c_{L,v}(t)$ is the actual value of the induced lift after the initiation of the diminishing effect. Hence, the total lift becomes

$$c_L(t) = c_{L,d}(t) + c_{L,v}(t); \tag{20}$$

see Fig. 6. This introduces one additional state variable $c_{L,v}(t)$ into the model. Furthermore, two profile dependent parameters are introduced, namely ω_4, which controls the diminishing rate of the vortex lift, and the critical angle α_v at

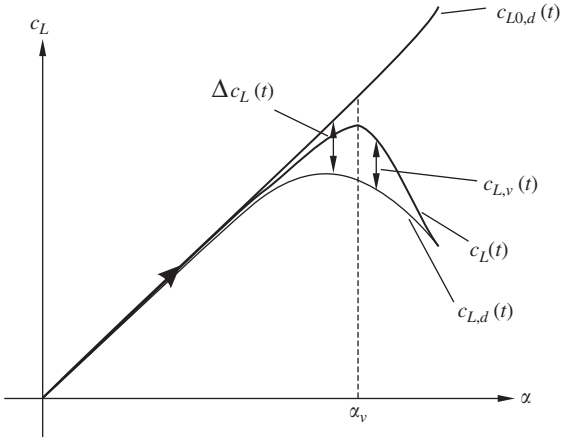

Fig. 6. Illustration of lift components used to described leading edge separation.

which the leading edge vortex detaches from the leading edge. Leishman and Beddoes (1986a, b) showed that α_v is dependent on the tip pressure, which can be determined from a delay of $c_{L0,d}$. This introduces an additional filter equation to account for the dynamics of the tip pressure. However, when considering the pitch rates of wind turbines the accuracy obtained from introducing an extra filter equation is relatively low considering the increased complexity and computational cost of the model. A variable τ is included to control the position of the travelling vortex. However, assuming the travel velocity being given, this will not introduce additional parameters to be calibrated. The dimensionless variable τ is equal to 0 when the travelling vortex is located at the leading edge and $\tau = 1$ when the vortex reaches the trailing edge. Assuming constant travel velocity, the time change of τ is given as

$$\dot{\tau} = \begin{cases} \dfrac{V}{3c} & \text{for } \alpha > \alpha_v, \\ 0 & \text{otherwise.} \end{cases} \tag{21}$$

When $\tau \geqslant 1$, the vortex detaches and stops building up strength. Finally, as $\dot{\alpha} < 0$ a new cycle starts and $\tau = 0$. These conditions give the following modification to Eq. (19):

$$\dot{c}_{L,v}(t) + \omega_4 c_{L,v}(t) = \begin{cases} \Delta\dot{c}_L(t) & \text{for } \tau < 1 \text{ and } \dot{\alpha} > 0, \\ 0 & \text{otherwise.} \end{cases} \tag{22}$$

It should be noted that the case of $\alpha(t)$ varying at high pitch rates around α_v produces the possibility of several vortices in the wake contributing to the lift, but only one can be located on the profile building up strength.

The influence on the moment coefficient from delayed circulation built-up and delayed separation may be included in Eq. (9) directly by replacing c_{L0} with $c_{L0,d}$ and f with f_d. However, the travelling vortex severely influences the movement of the centre of pressure, which increases the complexity of modelling the moment coefficient. The Beddoes–Leishman model includes a series of empirical expressions for determining the influence from the travelling vortex on the moment coefficient, see e.g. Leishman and Beddoes (1986a). Further, analyses are needed to understand the complexity of the travelling vortex on the aerodynamic loads, but this will not be further pursued here.

2.4. State variable formulation

The present model includes four state variables for every wing section at which the lift is calculated. Two variables c_1 and c_2 to describe the delayed linear lift, one variable θ_d to describe the dynamic movement of the separation angle and one variable $c_{L,v}$ to describe the induced lift from the pressure peak and vortex forming under leading edge separation. In matrix formulation, the linear differential equations describing these state variables can be organised as follows:

$$\dot{\mathbf{z}}(t) = \mathbf{A}\mathbf{z}(t) + \mathbf{b}_0(\alpha) + \mathbf{b}_1\dot{c}_{L0}(t), \tag{23}$$

where

$$\mathbf{z}(t) = \begin{bmatrix} c_1(t) \\ c_2(t) \\ \theta_d(t) \\ c_{L,v}(t) \end{bmatrix}, \quad \mathbf{A} = \begin{bmatrix} -\omega_1 & 0 & 0 & 0 \\ 0 & -\omega_2 & 0 & 0 \\ 0 & 0 & -\omega_3 & 0 \\ 0 & 0 & 0 & -\omega_4 \end{bmatrix}, \tag{24}$$

$$\mathbf{b}_0(\alpha) = \begin{bmatrix} 0 \\ 0 \\ \omega_3\theta(\alpha) \\ \Delta\dot{c}_L(t)H(\alpha_v - \alpha)H(\dot{\alpha}) \end{bmatrix}, \quad \mathbf{b}_1 = \begin{bmatrix} A_1 \\ A_2 \\ 0 \\ 0 \end{bmatrix}, \tag{25}$$

in which $H(x)$ is the unit step function. The total lift coefficient then follows from Eqs. (14), (17) and (20) as

$$c_L(t) = \cos^4(\tfrac{1}{4}\theta_d(t))[c_{L0}(\alpha) - c_1(t) - c_2(t)] + c_{L,v}(t). \tag{26}$$

The static coefficients to be determined are $c_{L0}(\alpha)$, $\dot{c}_{L0}(t)$ and $\theta(\alpha)$ which all can be found from experimental static lift coefficients. The first two are determined from the slope of $c_L(\alpha)$ at $\alpha = \alpha_0$, with the earlier mentioned modification at $f = 0$, where $c_{L0} = 4c_L$. $\theta(\alpha)$ is then found from Eq. (17). Furthermore, a series of profile dependent constants are used in the model. A_1, A_2, ω_1 and ω_2 are determined from fully attached conditions, i.e. on the linear part of the lift curve. For a thin plate profile, these parameters may be determined by an appropriate second-order filter approximation to the

Wagner function, see e.g. Jones (1940). For an actual profile, the parameters may be determined from dynamic test data at low angles of attack. ω_3, ω_4 and α_v may all be determined from dynamic test data at high angles of attack.

The delay flow conditions vary with the mean velocity V and the chord length of the profile c. It is often used to introduce nondimensional time variable depending on these quantities, see e.g. (Fung, 1993, p. 207). However, a convenient way of introducing these effects is to adopt the variation with V and c within the timescale parameters ω_j, $j = 1, 2, 3, 4$. This approach is also used by the Risø model described in Appendix A.4. The timescales of these models are all defined via the following nondimensional (reduced) parameter:

$$\hat{\omega}_j = \omega_j \frac{c}{2V}. \tag{27}$$

Similarly, the oscillation of the airfoil is characterised by the so-called reduced frequency $\hat{\omega}$ given as

$$\hat{\omega} = \omega \frac{c}{2V}, \tag{28}$$

where ω is the circular frequency of the oscillation.

3. Comparison of models

The main input to all the models are the quasi-static lift data. The dynamic stall models should be able to reproduce these in the entire range of α. At low reduced frequencies and at angles of attack below the point of full separation, all the models generate results close to the static lift curve. At angles of attack above this point, the Beddoes–Leishman model is no longer capable of reproducing static data, whereas the proposed model follow the static curve nicely due to the modification C_{L0}. This is illustrated in Fig. 7, where static data from a NACA 63-418 profile (Abbott and von Doenhoff, 1959) is extrapolated linear from 20° into the deep stall regime to the point $c_L(90°) = 0$.

The Beddoes–Leishman model also seems to perform badly at angles of attack just below fully separated flow conditions (approximately 32°), where the lift seems to curve away from the measured values. This is caused by the way the effective attachment degree is determined from the static data set, where linear interpolation is used in this simulation. The problem may be solved by using quadratic interpolation, which obviously is more time consuming. Within the proposed model, the same problems are avoided due to the complex mapping (6), which takes care of the square root singularity at $f = 0$.

In the following examples, the performance of the various models is validated against experimental results from wind-tunnel tests on a Vertol 23010-1.58 airfoil. The test results are presented by Liiva (1969), and are used to verify the Boeing–Vertol model (Tarzanin, 1972). The experimental data are produced for harmonic pitching of the airfoil at various mean angles of attack, the amplitude $\Delta\alpha$ is held constant at 4.85° and $\hat{\omega}$ is kept constant at 0.062, where $c = 1.5\,\text{m}$, $V = 60\,\text{m/s}$. Ideally, to calibrate the various models, a series of test data should be available at a range of reduced frequencies, amplitudes and mean values of oscillation. The rather limited set of test data makes the calibration of the parameters very uncertain, but the performance of the models may to some extent be analysed. Under fully

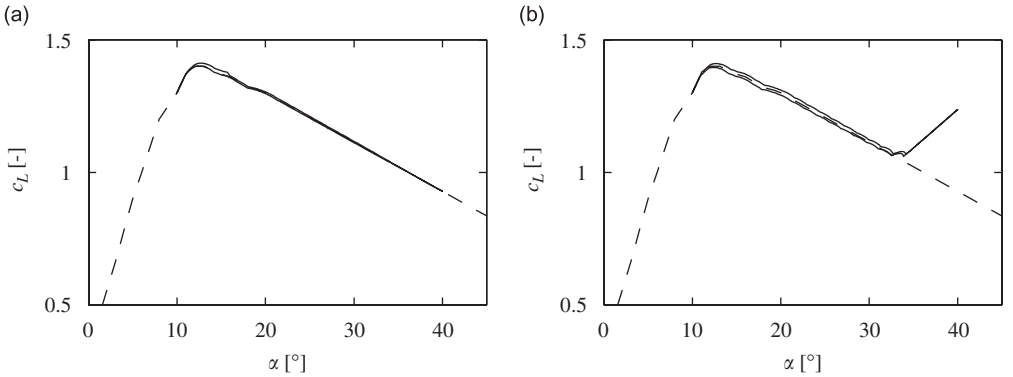

Fig. 7. Lift coefficient for a NACA 63-418 at low reduced frequency: $\hat{\omega} = 0.0005$; $\alpha_{\text{mean}} = 25°$; $\Delta\alpha = 15°$; ––, static test data. (a) —, Proposed model. (b) —, Beddoes–Leishman model.

Table 1
Profile dependent parameters for the various dynamic stall models determined from dynamic test data from Vertol 23010-1.58 profile

	Present	Beddoes–Leishman	ONERA	Øye	Risø	Boeing–Vertol
$\hat{\omega}_1$	0.0455	0.125	0.125	—	0.0455	—
$\hat{\omega}_2$	0.3	0.375	0.1	—	0.3	—
$\hat{\omega}_3$	0.1	0.275	—	0.07	0.0875	—
$\hat{\omega}_4$	0.075	0.075	—	—	—	—
$\hat{\omega}_5$	—	2.5	—	—	—	—
$\hat{\omega}_6$	—	2.5	—	—	—	—
$\hat{\omega}_7$	—	0.4	—	—	0.4125	—
A_1	0.165	0.3	0.3	—	0.165	0.87
A_2	0.335	0.7	0.1	—	0.335	—
A_3	—	1.0	—	—	—	—
A_4	—	1.0	—	—	—	—
α_v	14.75°	—	—	—	—	—
$c'_{L0,v}$	—	1.6	—	—	—	—
α_{sep}	—	—	—	32°	—	—
ζ	—	—	0.7	—	—	—

attached flow conditions the proposed model, the Beddoes–Leishman, the ONERA and the Risø models all perform well. For the present and Risø models, the incompressible parameters given by Jones (1940) are used. The parameters of the various models during stall conditions are calibrated by the least-square-error method between the model output and test data. The data points used in the least-square-error method are uniformly distributed, hence, all regions of the model are weighted equally. The calibrated parameter values are listed in Table 1. It is obvious that the Boeing–Vertol and the Øye models are relatively easy to calibrate since only a few parameters need to be identified. The present model has seven parameters, the Risø model has six parameters, the ONERA model has five parameters and the Beddoes–Leishman model has 12 parameters which need calibration. The many parameters of the Beddoes–Leishman model makes optimal calibration virtually impossible. Tran and Petot (1981) devised a method of calibrating the ONERA model from small amplitude, low- and high-frequency test data below and above stall. Since no such variety of test data have been available, the calibration is also done by the least-square-error method.

In Figs. 8 and 9, the various models are compared with experimental data from the Vertol 23010-1.58 profile. Test data indicated by the symbol $\times$, measured static data which serves as input are illustrated as dashed lines, and the results from the calibrated dynamic stall models using parameters given in Table 1 are plotted as full lines. From the top down in Fig. 8, the numerical results are plotted obtained from the proposed, Beddoes–Leishman and Risø models, and in Fig. 9 from the ONERA, Øye and Boeing–Vertol models. The cyclic direction of the experimental data are indicated by a $>$, whereas the cyclic direction of the numerical simulations are indicated by ▶. In all cases, the cyclic direction is indicated on the upper part of the curve, hence the arrows should point in the same direction. The subfigures to the left illustrate the results of a test situation under fully attached flow condition with a mean angle of attack of 7.33°. As seen, the proposed, Beddoes–Leishman, Risø and ONERA models capture the cyclic behaviour, whereas both the Øye and Boeing–Vertol models produce results which travel in the opposite direction to the test data. To illustrate the cyclic behaviour of the Øye and Boeing–Vertol models, a minor section of the curve is expanded in the lower right corner. The Øye and Boeing–Vertol models are not designed to account for the dynamics of the lift curve at fully attached flow conditions, and care should be exercised in this limiting case. To the right in Figs. 8 and 9, the mean angle of attack is increased to 14.92°, which is in the stall regime. All models capture the correct cyclic behaviour, but especially the Øye and the ONERA models predict a maximum lift which is approximately 10–15% below the measured value. The Øye model fails mainly because of no travelling vortex contribution, which is significant at high reduced frequencies. Especially, the Boeing–Vertol model captures the test data very effectively, but also the present, Risø and Beddoes–Leishman models perform well. It should be mentioned that the test data originally was used to verify the Boeing–Vertol model. The present and Beddoes–Leishman models predict the declining lift after the dynamic stall peak is too high. Leishman and Beddoes (1986b) suggest an increase of the vortex dissipation after the vortex leaves the profile, i.e. increasing ω_4. This modification will produce better results in this particular case for both the present and Beddoes–Leishman models. The Risø model predicts a maximum lift, which is a little below that of the two other models but still within an acceptable range. It should be noted that even though the state variable $c'_{L0,d}$ in the

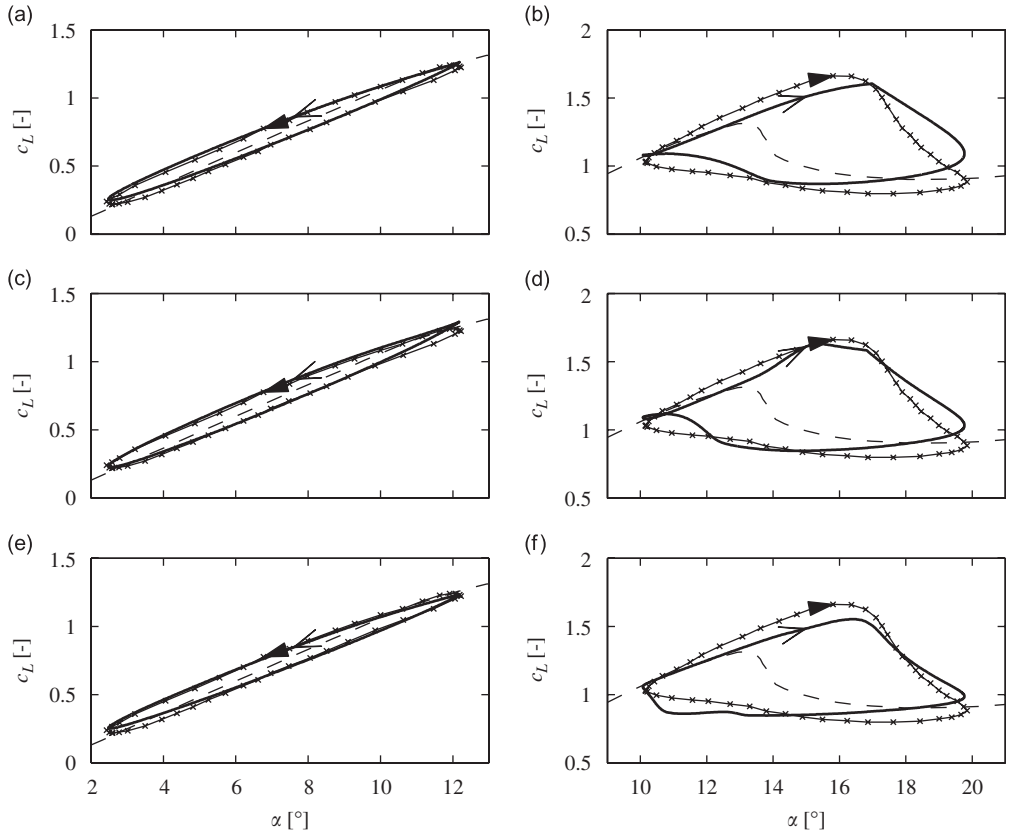

Fig. 8. Comparison between dynamic stall models and lift coefficient for a Vertol 23010-1.58 profile at various mean angles of attack. $\hat{\omega} = 0.062$. >, Cyclic direction of semi-empirical models. ▶, Cyclic direction of dynamic test data. ––, Static test data. ×, Dynamic test data. (a), (b) —, Present model. (c), (d) —, Beddoes–Leishman model. (e), (f) —, Risø model.

Beddoes–Leishman and the Risø model should describe the same effect, the calibrated parameter ω_3 are very different. This is due to the fact that the Risø model does not include contributions from leading edge separation, that is why these contributions are absorbed into the trailing edge separation state variables. As seen from Fig. 8f, this works nicely for the presented case.

Next, the performance of the present model is analysed. Fig. 10 shows the static values of c_{L0} and θ (dashed line) corresponding to the static lift coefficient from NACA 63-418. The reason for using the NACA 63-418 profile is to illustrate the variation of the static and dynamic variables also during fully separated flow conditions, which is not obtained within the angle of attack limits of the Vertol profile. A simulation of $c_{L0,d}$ and θ_d is shown as a full line. As seen, full separation occurs at approximately 32°, where $\theta = \pi$ and c_{L0} is changed from the linear approximation to $4c_L$.

Fig. 11 illustrate the performance of the present model at various variation of parameters. The static input (dashed line) is from the Vertol 23010-1.58 profile, and the light full line indicates a reference case using the parameters given in Table 1, column 2. In Fig. 11(a), the result of a simulation at low angles of attack in the fully attached flow domain is plotted. The heavy full line illustrates a simulation with $A_1 = 0.3$ and $A_2 = 0.7$ which match the compressible parameters of the Beddoes–Leishman model. Under compressible conditions, i.e. when $A_1 + A_2 = 1$, no instantaneously change in lift appears for a change of the angle of attack, which, as indicated in Fig. 11(a), results in a wider hysteresis loop at fully attached flow conditions. Figs. 11(b)–(d) illustrate numerical results during dynamic stall conditions with $\alpha_{\text{mean}} = 15°$ at variation of ω_3, ω_4 and α_v, respectively. As seen from Fig. 11(b), a change of ω_3 does not influence the maximum lift significantly. Also increasing ω_3 by 50% from the reference value (bold line) only introduces small deviations from the reference value. However, decreasing ω_3 by 50% (dashed line) introduces significant changes to the lift, both at flow reattachment at low angles of attack and also in the deep stall regime at high

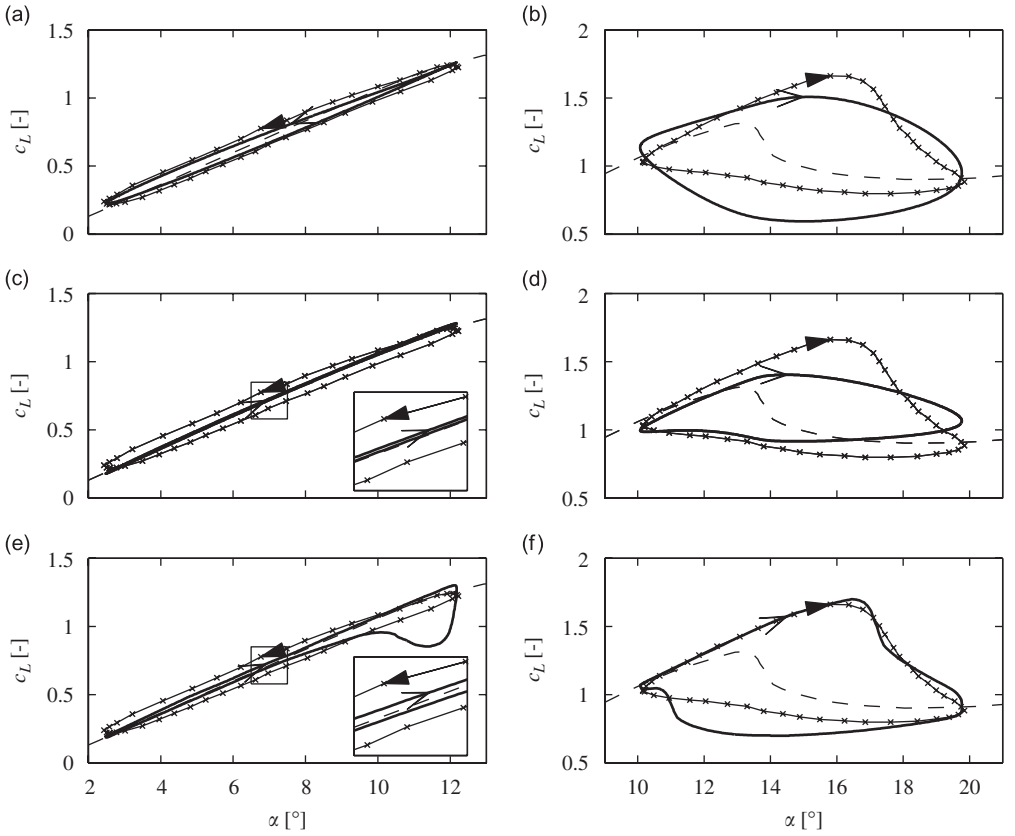

Fig. 9. Comparison between dynamic stall models and lift coefficient for a Vertol 23010-1.58 profile at various mean angles of attack. $\hat{\omega} = 0.062$. >, Cyclic direction of semi-empirical models. ▶, Cyclic direction of dynamic test data. ––, Static test data. ×, Dynamic test data. (a), (b) —, ONERA model. (c), (d) —, Øye model. (e), (f) —, Boeing–Vertol model.

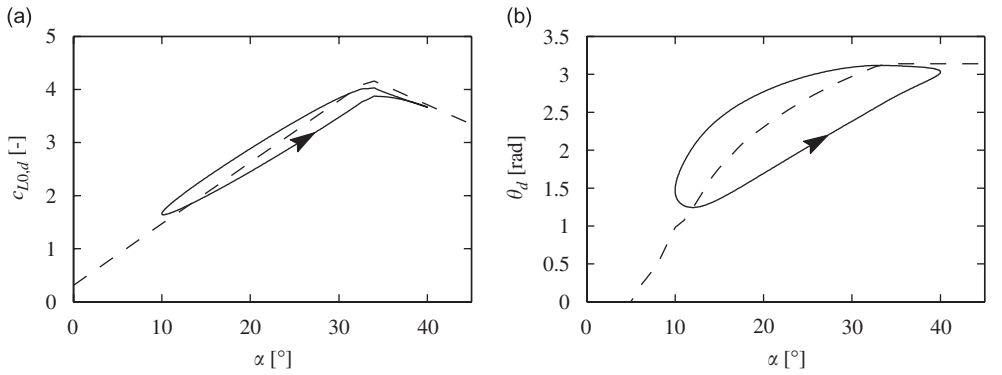

Fig. 10. State variables of the present model during dynamic stall cycle of a NACA 63-418 profile, $\hat{\omega} = 0.062$, $\alpha_{\text{mean}} = 25°$, $\Delta\alpha = 15°$. ––, Quasi-static component. (a) —, $c_{L0,d}$, (b) —, θ_d.

angles of attack. At low values of ω_3, small variations in the static lift is filtered out and the curve becomes smoother. Variations of ω_4 and α_v illustrated in Fig. 11(c) and (d), basically move the dynamic stall point up and down and sideways, respectively. In Fig. 11(c), the dynamic lift without the vortex contribution $c_{L,d}$ (bold dashed lines), the vortex contribution at these relatively high reduced frequencies is significant.

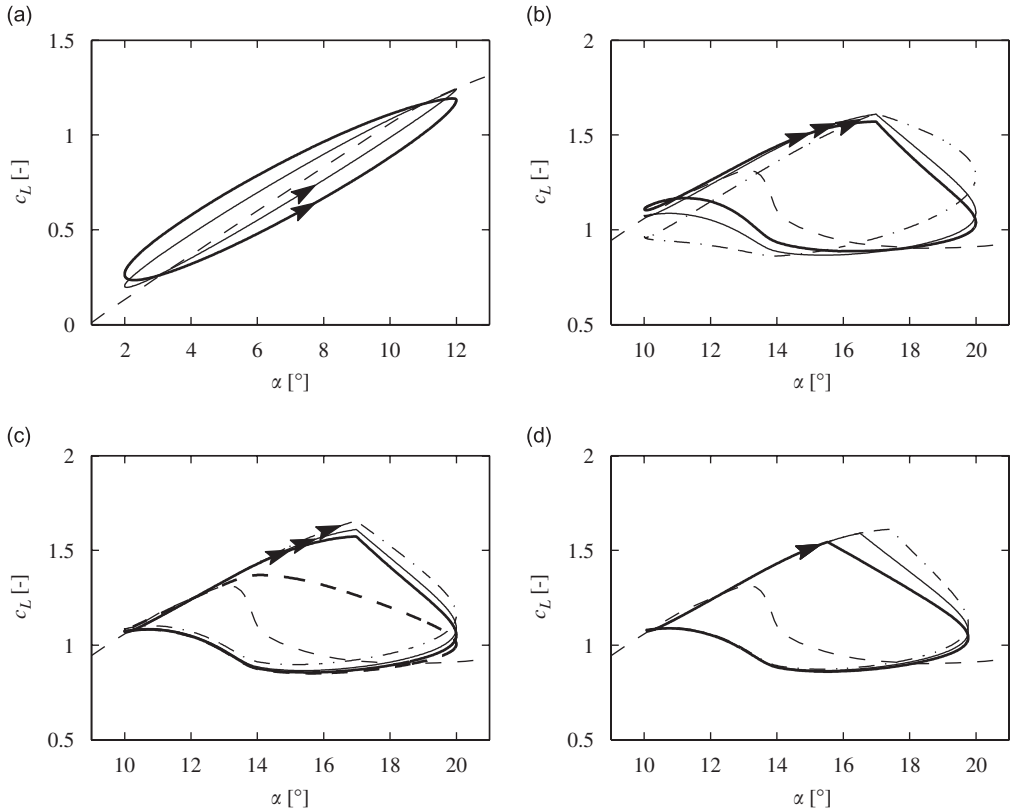

Fig. 11. Lift curve of the Vertol 23010-1.58 profile at various parameter values. $\hat{\omega} = 0.062$, $\Delta\alpha = 10°$. – –, Quasi-static component. —, reference case using the parameters of Table 1, column 2. (a) Variation of A_1 and A_2. $\alpha_{mean} = 7°$. —, $A_1 = 0.3$, $A_2 = 0.7$. (b) Variation of ω_3. $\alpha_{mean} = 15°$, —, $\omega_3 = 4$. –·–·, $\omega_3 = 12$. (c) Variation of ω_4. $\alpha_{mean} = 15°$. —, $\omega_4 = 4$. –·–·, $\omega_4 = 8$. – –, without $c_{L,v}$. (d) Variation of α_v. $\alpha_{mean} = 15°$. —, $\alpha_v = 13.75°$. – –, $\alpha_v = 15.75°$.

4. Other aspects of dynamic stall models

4.1. Aeroelastic modelling

All the indicated dynamic stall models are one-degree-of-freedom models in $\alpha(t)$. Assume that the profile has the translation velocities $\dot{u}'_1(t)$ and $\dot{u}'_2(t)$ in the blade and edgewise direction, respectively, the pitch velocity $\dot{\alpha}(t)$ around the aerodynamic centre A, and exposed to turbulence components $v'_1(t)$ and $v'_2(t)$. The flow conditions are illustrated in Fig. 12. Assuming the wavelength of the turbulence is significantly larger than the chord-length of the profile, the structural deformation velocities and turbulence components will introduce a uniform flow change over the entire profile. However, the pitch motion introduces a linear flow variation over the section. These effects are included through the introduction of an equivalent angle of attack $\alpha_{eq}(t)$. From the profile, the deformation velocities and turbulence components can be regarded as a variation of the incoming velocity field; however, due to the flow variation over the profile from the pitch velocity, this contribution cannot be included directly. Under fully attached flow conditions with the profile moving in both heaving and pitching motions, it can be shown that $\alpha_{eq}(t)$ should be found from the downwash velocity at the $\frac{3}{4}c$ point for the flow to follow the profile and separate at the trailing edge fulfilling the so-called Kutta condition, see (Fung, 1993, pp. 401). This is illustrated in Fig. 12.

Including turbulence components and deformation velocities as variation of the mean wind gives the following expression for α_{eq}:

$$\sin\alpha_{eq}(t) = \frac{V'_1(t) + v'_1(t) - \dot{u}'_1(t) + (c/2)\dot{\alpha}(t)}{V(t)}, \tag{29}$$

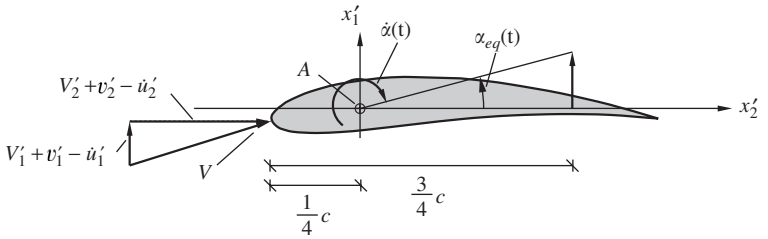

Fig. 12. Definition of α_{eq}.

where $V(t)$ is the resulting wind speed including contributions from both turbulence components and deformations velocities. This gives the following linearised expression for $\alpha_{eq}(t)$:

$$\alpha_{eq}(t) \simeq \alpha(t) + \frac{c}{2V}\dot{\alpha}(t) + \frac{v_1'(t) - \dot{u}_1'(t)}{V(t)}, \tag{30}$$

where $\alpha(t)$ is the mean wind contributions to the angle of attack. In Eq. (30), it is presumed that $\dot{u}_1'(t)$, $v_1'(t)$, $\alpha(t)$ and $\dot{\alpha}(t)$ are sufficiently small, so that linearisation is possible. Even though only valid under fully attached flow, it is common practice to determine $\alpha_{eq}(t)$ from the downwash at the $\frac{3}{4}c$-point under separated flow conditions. Now, $\alpha(t)$ in Eq. (25) is simply replaced with $\alpha_{eq}(t)$ to introduce aeroelastic contributions.

4.2. Camber and thickness

The backbone curve given in Eq. (3) is derived for a thin plate section. Krenk (2006) derived the following expression for the static lift curve in terms of separation for a wing section with a camber line $y(x)$ and a thickness distribution $h(x)$ given as polynomials of the following form:

$$y(x) = y_0\left(1 - \left(\frac{x}{a}\right)^2\right), \quad h(x) = h_0\sqrt{\frac{a+x}{2a}}\frac{a-x}{a}, \tag{31}$$

where a is the half-chord length $a = c/2$, y_0 and h_0 define the camber and thickness at $x = 0$, respectively. In linearised airfoil theory, it can be shown that the effect of camber and thickness is to change the zero lift angle, while the effect of separation enters via the zero lift angle and the same factor as for the flat plate (Krenk, 2006). The lift force is then given as

$$c_L = \left(\frac{1+\sqrt{f}}{2}\right)^2\left(c_{L0} - \left.\frac{\partial c_L}{\partial\alpha}\right|_{\alpha_0}\alpha_L(f)\right), \tag{32}$$

where c_{L0} is the lift at fully attached flow defined by $f = 1$. As was the case of the thin plate model, special measures need to be taken when fully separated conditions occur ($f = 0$), again this is done by modifying c_{L0} as

$$c_{L0} = \begin{cases} \left.\dfrac{\partial c_L}{\partial\alpha}\right|_{\alpha_0}\left(\alpha + \dfrac{y_0}{a}\right), & f > 0, \\ 4c_L - \left.\dfrac{\partial c_L}{\partial\alpha}\right|_{\alpha_0}\dfrac{3}{4}\left(\dfrac{y_0}{a} - \dfrac{h_0}{a}\right), & f = 0, \end{cases} \tag{33}$$

where c_L in the second line of Eq. (33) is a measured value. The last term in the first line of Eq. (33) is the zero lift angle at fully attached flow conditions. The angle α_L is a modification of the zero lift angle due to separation defined as

$$\alpha_L = -\frac{3}{4}(1 - 6\sqrt{f} + 5f)\frac{y_0}{a} + \frac{3}{4}(1 - \sqrt{f})\frac{h_0}{a}. \tag{34}$$

Inverting Eq. (32) gives f in terms of c_L as a fourth-degree polynomial in $\sqrt{f}$. The dynamic lift is then found by delaying c_{L0} according to Eqs. (13) and (14), and f according to Eq. (16), and inserting in Eqs. (32) and (34). The effects from leading edge separation may be added as an additional term to c_L according to Eq. (20).

The formulation Eqs. (32)–(34) differs in notation from the formulation of Krenk (2006). Two considerations are made. Firstly, c_L should be equal to c_{L0} for fully attached flow conditions, i.e. $f = 1$. Secondly, c_L on the left-hand side of Eq. (32) should be equal to measured values of c_L for fully separated flow conditions, i.e. $f = 0$. Both are ensured when c_{L0} and α_L are given as Eqs. (33) and (34), respectively, which correspond to Eq. (4) for the thin plate.

A single case is considered to illustrate the effects of camber and thickness. The section shape is illustrated in Fig. 13. The thin plate profile is used with $y_0 = h_0 = 0$ as a reference case. The same shape of the measured static data is used for both cases. The numerical results for simulations using a harmonic variation of α with amplitude 8° and mean value located at $\alpha = 8^\circ$ and 20°, respectively, are illustrated in Fig. 14. In the figure the thin plate reference case is indicated by dashed lines, with thin dash lines indicating the static curve and thick ones indicating the results from harmonic variation of α. For $y_0 = 0$ inserted in Eq. (32) gives zero lift at $\alpha = 0$, and the effect of camber effectively translates the

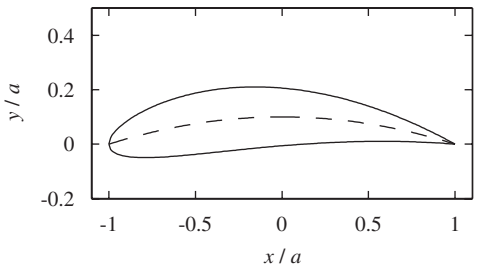

Fig. 13. Section shape: $y_0 = 0.1\,\text{m}$, $h_0 = 0.15\,\text{m}$.

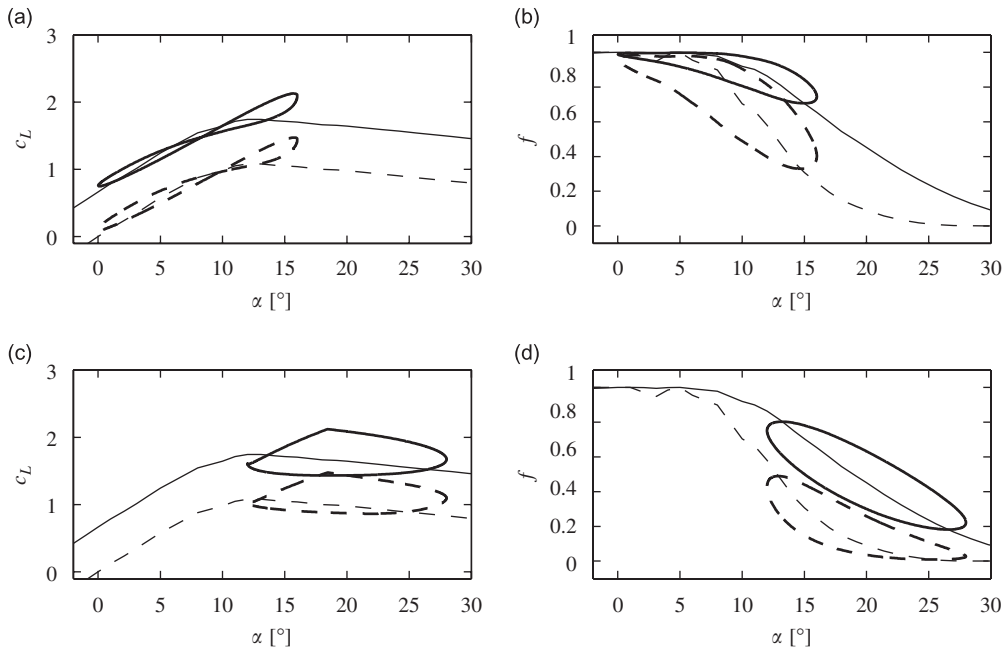

Fig. 14. Results for profile with camber $y_0 = 0.1\,\text{m}$ and thickness $h_0 = 0.15\,\text{m}$. ––, Static data reference case. —, dynamic data reference case. —, Static data camber and thickness profile. —, dynamic data camber and thickness profile. (Left) $c_L(\alpha)$. (Right) $f(\alpha)$. (a), (b) $\alpha_m = 8^\circ$. (c), (d) $\alpha_m = 20^\circ$.

backbone curve. The dynamic lift is translated with the backbone curve, however the shape is relatively unaffected by camber. The thickness distribution introduces significant changes of the static degree of attachment. However, the effective changes on the shape of the dynamic lift curve are minimal because the backbone curve also changes with h_0. Thus, thickness only introduces minor changes to the dynamic lift curve, while camber effectively translates the backbone curve. The same effect can approximately be obtained to an acceptable degree by using the flat plate reduction of the lift due to separation given in Eq. (3) and the measured profile data for the cambered profile as backbone curve.

The moment coefficient for the thin plate is given in Eq. (9). However, both camber and thickness influence the movement of the centre of pressure due to separation. Krenk (2006) obtained the following expression for the moment coefficient for the considered profile:

$$c_M = \frac{\pi}{2}\left(\frac{1+\sqrt{f}}{2}\right)^2 \left\{ \left[1 - \frac{1}{4}(1 - 6\sqrt{f} + 5f)\right]\alpha - \left(\frac{1-\sqrt{f}}{2}\right)^2 \left[(1 + 6\sqrt{f} + 25f)\frac{y_0}{a} + \frac{3}{2}(1 - 3\sqrt{f})\frac{h_0}{a}\right] \right\}. \tag{35}$$

As seen, camber and thickness do not contribute to the moment coefficient at fully attached flow, but introduce a change in moment as the attachment decreases. Also, the effects of camber and thickness appear merely as additions to the thin plate solution.

5. Concluding remarks

In the present work, a model for determining the dynamic lift coefficient of a wind turbine wing profile has been developed, based on the effects of various flow conditions. In the model three basic features have been included. Firstly, a time delay is introduced under fully attached flow situations using two filter equations. Secondly, the time delay in the motion of the separation point is described by one filter equation. And last, a contribution from leading edge separation vortex and pressure peak is included by one filter equation.

The characteristics of the present model are a simplified description of attached flow, calculating lift by analytical linearised flow theory in the entire range of the angle of attack and inclusion of a contribution from leading edge separation. Additionally, a modified model for the delay on the attachment degree has been suggested, which operates on a mapping of the profile onto a circle in the complex plane.

The model has been validated against dynamic test data of the Vertol 23010-1.58 profile. It should be emphasised that the available experimental data for calibration of the various models have been limited, and thus the calibrated model parameters are intended to illustrate the ability of the model to represent the basic dynamic load phenomena, and not to serve as general properties of wind turbine profiles. It has been demonstrated that the present model is capable of producing the correct cyclic behaviour of the lift under fully attached conditions. Also, under a dynamic stall cycle, the present model is capable of modelling the maximum lift and reproducing lift data to a satisfactory degree. A variety of different approaches of modelling dynamic stall has been described including the Beddoes–Leishman, Risø, ONERA, Øye and Boeing–Vertol methods. Only the present model, Risø and Beddoes–Leishman models are capable of reproducing the experimental data both at fully attached flow conditions and in the stall regime. Seven parameters are introduced in the present model compared to twelve in the Beddoes–Leishman model making calibration considerably less complicated. The Risø model introduces an interpolation scheme comparable to that devised of the Øye model to introduce the effects of trailing edge separation. Further, it includes an extra state variable to model trailing edge separation. However, the present model performs equally well using only one state variable for trailing edge separation and introducing an extra state variable to account for leading edge separation. Hence, the model presented here includes additional contributions without increased computational costs.

The effects of camber and thickness have been analysed and it was found that camber introduces a significant increase in lift; however, this effect may be included as a translation of the backbone curve for the thin plate model. Only minor effects are observed from introducing thickness into the backbone formulation.

Finally, when assuming the position of the separation point to be known, the moment coefficient can be found explicitly by use of linearised airfoil theory both for the thin plate and actual profile with camber and thickness. Dynamic variation of the moment can be introduced directly when considering delayed separation, however the effects of the travelling vortex on the centre of pressure have not been analysed, and further work should be done.

Acknowledgement

The present work has been supported by the Danish Technical Research Council within the project "Damping Mechanisms in Dynamics of Structures and Materials".

Appendix A. Other dynamic stall models

A.1. Beddoes–Leishman model

The Beddoes–Leishman model presented in what follows has been developed with the main purpose of calculating lift loads on helicopter profiles, (Leishman, 1988, 2000; Leishman and Beddoes, 1986a, b; Beddoes, 1978). This semi-empirical model takes into account the effect of flow compressibility under high-frequency movements. Additionally, the model includes time delays under attached flow, and the contribution to the load coefficient from a discrete vortex forming under leading edge separation. The model also describes the dynamic variation of moment and drag forces, but only the lift model is included explicitly here.

Under fully attached flow conditions, where the load response is basically linear, the time delays of the lift coefficient are modelled by the following relation:

$$c_{L0,d}(t) = c_{L0}(\alpha) - c_1(t) - c_2(t) + c_3(t) + c_4(t), \tag{A.1}$$

where $c_3(t)$ and $c_4(t)$ are impulsive contributions diminishing in time due to wave propagation. Beddoes and Leishman give the following expression for finding the impulsive contributions:

$$\dot{c}_3 + \omega_5 c_3 = \frac{4}{M} A_3 \dot{\alpha}, \quad \dot{c}_4 + \omega_6 c_4 = \frac{1}{M} A_4 \frac{c}{V} \ddot{\alpha}. \tag{A.2}$$

M is the Mach number given as $M = V/V_0$, with V_0 the speed of sound; $c_1(t)$ and $c_2(t)$ are determined from Eq. (13) with $A_1 + A_2 = 1$. It should be noticed that while $c_1(t)$ and $c_2(t)$ are found using $\alpha_{\mathrm{eq}}(t)$, $c_3(t)$ and $c_4(t)$ should be found using the actual pitch rate $\dot{\alpha}$ and pitch acceleration $\ddot{\alpha}$.

To determine the dynamic attachment degree f_d, two state variables are introduced in the following way. First a retarded linear lift $c'_{L0,d}(t)$ is introduced as a delayed state variable of the linear lift $c_{L0,d}(t)$, which should give a one-to-one correspondence between the pressure coefficient and the dynamic lift at changing pitch rates. The following differential equation is used for $c'_{L0,d}(t)$:

$$\dot{c}'_{L0,d}(t) = -\omega_7 (c'_{L0,d}(t) - c_{L0,d}(t)). \tag{A.3}$$

An effective angle of attack $\alpha_f = c'_{L0,d}(t)/(dc_L/d\alpha)|_{\alpha_0} + \alpha_0$ is then used to find the actual static attachment degree by which f_d can be found from Eq. (16) substituting α with α_f. Inserting the dynamic linear lift coefficient $c_{L0,d}$ and attachment degree f_d into Eq. (3) gives the dynamic lift coefficient. Notice that the Beddoes–Leishman model uses the approach of a modified angle of attack, which falls into the third group of models.

The approach for finding the leading edge separation contribution to the lift is similar to that described in Eqs. (18) and (19). Beddoes and Leishman relate this contribution to the discreet vortex forming as the flow separates. When a certain pressure level is reached at the leading edge, the vortex is said to separate and start moving across the profile. Hence, when $c'_{L0,d}$ is increased above a critical value, here named $c'_{L0,v}$, the vortex starts to move with a velocity $V/3$. As it reaches the trailing edge it is released into the wake, after which $\Delta\dot{c}_L(t) = 0$.

Thus, one extra profile dependent parameter is introduced to describe the leading edge contribution, namely the critical retarded lift $c'_{L0,v}$ and the travel velocity of the vortex. Beddoes (1978) found that the travel velocity of the vortex at low Mach number is approximately $V/3$.

The Beddoes–Leishman model includes seven state variables for every wing section at which the lift is calculated. Four variables c_1, c_2, c_3 and c_4 to describe the delayed linear lift, two variables $c'_{L0,d}$ and f_d to describe the dynamic movement of the separation angle and one variable $c_{L,v}$ to describe the induced lift from the vortex forming under leading edge separation. In matrix formulation the linear differential equations describing these state variables can be organised as follows:

$$\dot{\mathbf{z}}(t) = \mathbf{A}\mathbf{z}(t) + \mathbf{b}_0(\alpha, \dot{\alpha}, \ddot{\alpha}) + \mathbf{b}_1 \dot{c}_{L0}(t), \tag{A.4}$$

where

$$\mathbf{z}(t)=\begin{bmatrix} c_1(t)\\ c_2(t)\\ c_3(t)\\ c_4(t)\\ c'_{L0,d}(t)\\ f_d(t)\\ c_{L,v}(t)\end{bmatrix},\quad \mathbf{A}=\begin{bmatrix} -\omega_1 & 0 & 0 & 0 & 0 & 0 & 0\\ 0 & -\omega_2 & 0 & 0 & 0 & 0 & 0\\ 0 & 0 & -\omega_5 & 0 & 0 & 0 & 0\\ 0 & 0 & 0 & -\omega_6 & 0 & 0 & 0\\ -\omega_7 & -\omega_7 & \omega_7 & \omega_7 & -\omega_7 & 0 & 0\\ 0 & 0 & 0 & 0 & 0 & -\omega_3 & 0\\ 0 & 0 & 0 & 0 & 0 & 0 & -\omega_4\end{bmatrix},$$

$$\mathbf{b}_1=\begin{bmatrix} A_1\\ A_2\\ 0\\ 0\\ 0\\ 0\\ 0\end{bmatrix},\quad \mathbf{b}_0(\alpha,\dot{\alpha},\ddot{\alpha})=\begin{bmatrix} 0\\ 0\\ \frac{4}{M}A_3\dot{\alpha}\\ \frac{1}{M}A_4\frac{c}{V}\ddot{\alpha}\\ \omega_7 c_{L0}(\alpha)\\ \omega_3 f(\alpha_f)\\ \Delta\dot{c}_L(t)H(1-\tau)H(\dot{\alpha})\end{bmatrix}, \tag{A.5}$$

where τ is a dimensionless variable describing the placement of the leading edge separation vortex. For the vortex placed at the leading and trailing edge, $\tau=0$ and 1, respectively. The time change of τ, for a travel velocity of the vortex at $V/3$, can be found as

$$\dot{\tau}=\frac{V}{3c}H(c'_{L0,d}-c'_{L0,v}). \tag{A.6}$$

The total lift coefficient then follows from the state variables as

$$c_L(t)=\left(\frac{1+\sqrt{f_d(t)}}{2}\right)^2[c_{L0}(\alpha)-c_1(t)-c_2(t)+c_3(t)+c_4(t)]+c_{L,v}(t), \tag{A.7}$$

where $f_d(t)$ is a function of $c'_{L0,d}(t)$ through α_f.

A.2. ONERA model

The ONERA model (Tran and Petot, 1981) is based on the characteristics of the lift curve. The same arguments and system of equations are used for dealing with the drag and moment curves. Here we first assume that the lift is independent of the Mach number and that the difference between the unsteady and steady lift coefficients is small. A classical way, which is also adopted in the previously described models, is to introduce the history effects of the lift as a differential equation. A functional dependence between $c_{L,d}$, α, and the time derivatives of up to order N of both is postulated, as follows:

$$A(c_{L,d},\alpha,\dot{c}_{L,d},\dot{\alpha},\ddot{c}_{L,d},\ddot{\alpha},\ldots)=0. \tag{A.8}$$

The function A is nonlinear, since it is assumed to describe the dynamic stall behaviour. However, it is assumed that the dynamic lift may be linearised around the static lift $c_{L,s}$ at α, corresponding to the first-order Taylor expansion

$$\frac{\partial A}{\partial c_{L,d}}(c_{L,d}-c_{L,s})+\frac{\partial A}{\partial \dot{c}_{L,d}}\dot{c}_{L,d}+\frac{\partial A}{\partial \ddot{c}_{L,d}}\ddot{c}_{L,d}+\cdots+\frac{\partial A}{\partial \dot{\alpha}}\dot{\alpha}+\frac{\partial A}{\partial \ddot{\alpha}}\ddot{\alpha}+\cdots=0, \tag{A.9}$$

where it has been used that $A(c_{L,d},\alpha,0,0,\ldots)=0$. This linearisation is only valid for small changes of the angle of attack with small deviations between the dynamic and static lift. During a dynamic stall cycle, these variations may become rather large, but comparison with experimental data seems to justify Eq. (A.9). Derivatives with respect to α of higher order than two may be neglected, and in terms of frequencies one real pole and two complex conjugated poles seem to capture the characteristics of the lift. Hence, derivatives of higher order than three with respect to $c_{L,d}$ may be neglected.

This reduces Eq. (A.9) to

$$\frac{\partial A}{\partial c_{L,d}} c_{L,d} + \frac{\partial A}{\partial \dot{c}_{L,d}} \dot{c}_{L,d} + \frac{\partial A}{\partial \ddot{c}_{L,d}} \ddot{c}_{L,d} + \frac{\partial A}{\partial \dddot{c}_{L,d}} \dddot{c}_{L,d} = \frac{\partial A}{\partial c_{L,d}} c_{L,s} - \frac{\partial A}{\partial \dot{\alpha}} \dot{\alpha} - \frac{\partial A}{\partial \ddot{\alpha}} \ddot{\alpha}. \tag{A.10}$$

Additionally, the following observations are made. At low angles of attack, in the linear regime, measured frequency response functions are smooth and continuous. By contrast, in the stall regime, rapid variations are registered. The first statement leads to the conclusion that in the linear regime the lift may be modelled by a first-order differential equation with one real negative pole. In the stall area the lift development may then be modelled as a second-order differential equation with two complex conjugated poles with negative real part. The derivatives of A in Eq. (A.10) are further assumed to be time independent. This leads to the following set of equations:

$$\dot{c}_1 + \omega_1 c_1 = \omega_1 c_{L0} + (\omega_1 B_1 + B_2)\dot{\alpha} + B_1 \ddot{\alpha}, \tag{A.11}$$

$$\ddot{c}_2 + 2\zeta\omega_2 \dot{c}_2 + \omega_2^2 (1 + \zeta^2) c_2 = -\omega_2^2 (1 + \zeta^2)(\Delta c_L + B_3 \Delta \dot{c}_L), \tag{A.12}$$

$$c_{L,d} = c_1 + c_2, \tag{A.13}$$

where $\Delta c_L = c_{L0} - c_{L,s}$. Eq. (A.11) accounts for the negative real pole $-\omega_1$ and Eq. (A.12) accounts for the complex conjugated poles $-\zeta\omega_2 \pm \mathrm{i}\omega_2$. The right-hand side of Eq. (A.12) ensures that the complex conjugated poles only affect the solution in the stall regime, where $\Delta c_L \neq 0$. In the static limit $c_1 = c_{L0}$ and $c_2 = -\Delta c_L$ giving $c_{L,d} = c_{L0} - (c_{L0} - c_{L,s}) = c_{L,s}$.

It is assumed that the memory effect on the circulation built-up is modelled by a single first-order filter, rather than the two first-order filters used in the proposed model. Then it is possible to express the differential equation for $c_{L0,d}(t)$, using the first two terms of Eq. (12) inserted in Eq. (11) and differentiating with respect to time. This gives

$$\dot{c}_{L0,d} + \omega_1 c_{L0,d} = \omega_1 c_{L0} + (1 - A_1)\frac{\partial c_L}{\partial \alpha}\dot{\alpha}. \tag{A.14}$$

Comparing Eqs. (A.14) and (A.11) reveals that for a first-order filter the dynamic lift is uninfluenced by $\ddot{\alpha}$. Hence, $B_1 = 0$ and $B_2 = (1 - A_1)\partial c_L/\partial\alpha$. It should be noticed that the ONERA model, as is the case for the proposed model and the Beddoes–Leishman model, includes a contribution from $\Delta\dot{c}_L$. The first two models relate this contribution to the leading edge vortex build-up.

Small amplitude oscillations in the linear regime make it possible to determine the variables ω_1 and B_2. With these known, small amplitude oscillations in the stall regime are used to determine the parameters ζ, ω_2 and B_3. The performance of the model should then be verified from large amplitude oscillations at various frequencies.

Finally, the state formulation of the ONERA model reads

$$\dot{\mathbf{z}} = \mathbf{A}\mathbf{z} + \mathbf{b} + \mathbf{B}\boldsymbol{\alpha}, \tag{A.15}$$

$$\mathbf{z} = \begin{bmatrix} c_1 \\ c_2 \\ \dot{c}_2 \end{bmatrix}, \quad \mathbf{A} = \begin{bmatrix} -\omega_1 & 0 & 0 \\ 0 & 0 & 1 \\ 0 & -2\zeta\omega_2 & -\omega_d \end{bmatrix}, \quad \boldsymbol{\alpha} = \begin{bmatrix} \alpha \\ \dot{\alpha} \end{bmatrix},$$

$$\mathbf{b} = \begin{bmatrix} 0 \\ 0 \\ \omega_d c_L \end{bmatrix}, \quad \mathbf{B} = \begin{bmatrix} \omega_1 \left.\dfrac{\partial c_L}{\partial \alpha}\right|_{\alpha_0} & (1 - A_1)\left.\dfrac{\partial c_L}{\partial \alpha}\right|_{\alpha_0} \\ 0 & 0 \\ -\omega_d^2 \left.\dfrac{\partial c_L}{\partial \alpha}\right|_{\alpha_0} & -\omega_d^2 A_2 \left(\left.\dfrac{\partial c_L}{\partial \alpha}\right|_{\alpha_0} - \left.\dfrac{\partial c_L}{\partial \alpha}\right|_{\alpha} \right) \end{bmatrix},$$

$$c_{L,d} = c_1 + c_2, \tag{A.16}$$

where $\omega_d = \omega_2\sqrt{1 + \zeta^2}$ and B_3 is changed to A_2 for consistency in notation. It should be noticed that the second term of row three, column two of $\mathbf{B}$ includes the slope of c_L at the present angle of attack. The ONERA model includes three state variables and five unknown parameters, ω_1, ω_2, A_1, A_2 and ζ, to be determined from experimental data.

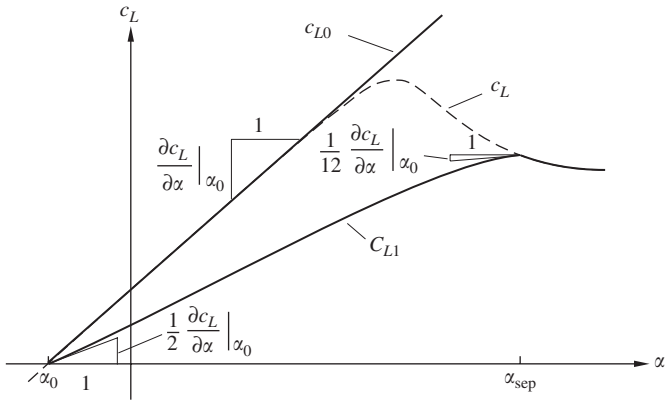

Fig. 15. Interpolation curves in the Øye model.

A.3. Øye model

As mentioned, the nonlinearity in the aeroelastic load model is essentially due to the motion of the separation point on the suction side of the profile. Øye (1991) has suggested a simple linear first-order filter model, which is based on the same static data requirements as the Beddoes–Leishman model and the proposed model. The essence of the Øye model is that relationship (3) for finding f is replaced by an interpolation between the lift coefficient at fully attached flow $c_{L0}(\alpha)$ determined from Eq. (2) and the static lift coefficient $c_{L1}(\alpha)$ at fully separated flow, corresponding to attachment degrees $f = 1$ and 0, respectively. The flow is defined to be fully separated at a given large angle of attack, α_{sep}, so $f = 0$ for $\alpha \geqslant \alpha_{sep}$. Øye assumes that the initial and final slopes of $c_{L1}(\alpha)$ may be chosen as $\partial c_{L1}/\partial\alpha|_{\alpha_0} = \frac{1}{2} dc_L/d\alpha|_{\alpha_0}$ and $\partial c_{L1}/\partial\alpha|_{\alpha_{sep}} = \frac{1}{12} dc_L/d\alpha|_{\alpha_0}$. Intermediate values of $c_{L1}(\alpha)$ are determined by Hermite interpolation. The interpolation curves c_{L0} and c_{L1} are shown in Fig. 15. Then, for $\alpha < \alpha_{sep}$, the static attachment degree f is determined by linear interpolation between the functional values $c_{L0}$and c_{L1}, i.e.

$$f = \frac{c_L - c_{L1}}{c_{L0} - c_{L1}}. \tag{A.17}$$

Using f in Eq. (16), the dynamic attachment degree can be found. Øye suggests that a value of $\omega_3 = V/4c$ can be used (Øye, 1991). Finally, the dynamic lift coefficient is determined from Eq. (A.17) by substituting f with f_d giving

$$c_L(t) = f_d(t)c_{L0} + (1 - f_d(t))c_{L1}. \tag{A.18}$$

The Øye model is based on only one state variable $f_d(t)$, which introduces the dynamic effects under dynamic stall. However, no dynamic effects are introduced during attached flow conditions. Four parameters are introduced: the initial and final slopes of c_{L1}, the timescale parameter ω_3 and the angle of attack defining full separation α_{sep}. The first two are defined by Øye and are assumed to be profile independent. Hence, two profile dependent parameters need calibration.

A.4. Risø model

The Risø model developed by Hansen et al. (2004) at Risø National Laboratory, Denmark, is a modified version of the Beddoes–Leishman model using only four state variables: two to model the unsteady lift for attached flow conditions, and two to model the dynamics of trailing edge separation. Leading edge separation and the dynamics between the travelling and trailing edge vortices are disregarded in this model. Also, dynamic models for moment and drag have been formulated but will not be described in the following.

An approach similar to the Øye model is used to model the nonlinear quasi-static lift. Assuming knowledge of the separation point and the lift under fully attached flow and fully separated flow conditions, respectively, the lift is given by

$$c_L = fc_{L0} + (1 - f)c_{L1}. \tag{A.19}$$

The linear lift c_{L0} is found from the lift slope at α_0, and the position of the separation point given by f is evaluated from Eq. (3). The restriction is that if f as determined from Eq. (3) is larger than 1.0, it is set equal to 1.0, and when full

separation occurs, f is set equal to 0. From a given set of measured c_L, f is found from Eq. (3) and c_{L1} may be determined from Eq. (A.19). Inverting Eq. (A.19) creates a singularity at $f = 1$, i.e. at fully attached flows. Under such conditions, c_{L1} is set to half the linear lift, i.e. $c_{L1}(f = 1) = c_{L0}/2$.

To introduce dynamic effects f and c_{L0} are modified, as was the case for the proposed model, Beddoes–Leishman model and Øye model. Under fully attached flow conditions, the Risø model works on a modified angle of attack instead of directly on the linear lift. The dynamic angle of attack α_d is given as

$$\alpha_d(t) = \alpha(1 - A_1 - A_2) + c_1(t) + c_2(t), \tag{A.20}$$

where

$$\dot{c}_i + \left(\omega_i + \frac{\dot{V}}{V}\right) c_i = \omega_i A_i \alpha. \tag{A.21}$$

Now the dynamic linear lift is evaluated as

$$c_{L0,d} = c_{L0}(\alpha_d) + \frac{\pi c \dot{\alpha}}{2V}. \tag{A.22}$$

The Risø model includes the most important contribution from added mass. This term does not introduce additional state variables or parameters to be calibrated; hence, it may easily be included in any of the other models. To introduce dynamic effects on the separation point motion, the same approach as the Beddoes–Leishman model is used. A retarded linear lift $c'_{L0}(t)$ is found from Eq. (A.3), an effective angle of attack, not to be compared with the equivalent angle of attack described in Section 4, is found as $\alpha_f = c'_{L0}/(dc_L/d\alpha)|_{\alpha_0} + \alpha_0$, and the delayed separation point f_d is determined from Eq. (16). This introduces two additional state variables: c'_{L0} and f_d. In state space formulation the Risø may be written as follows:

$$\dot{\mathbf{z}} = \mathbf{A}\mathbf{z} + \mathbf{b}, \tag{A.23}$$

$$\mathbf{z} = \begin{bmatrix} c_1 \\ c_2 \\ c'_{L0} \\ f_d \end{bmatrix}, \quad \mathbf{A} = \begin{bmatrix} -\left(\omega_1 + \frac{\dot{V}}{V}\right) & 0 & 0 & 0 \\ 0 & -\left(\omega_2 + \frac{\dot{V}}{V}\right) & 0 & 0 \\ 0 & 0 & -\omega_7 & 0 \\ 0 & 0 & 0 & -\omega_3 \end{bmatrix},$$

$$\mathbf{b} = \begin{bmatrix} \omega_1 A_1 \alpha \\ \omega_2 A_2 \alpha \\ \omega_7\left(c_{L0}(\alpha_d) + \frac{\pi c \dot{\alpha}}{2V}\right) \\ \omega_3 f(\alpha_f) \end{bmatrix}, \tag{A.24}$$

$$c_{L,d}(t) = f_d(t) c_{L0}(\alpha_d) + (1 - f_d) c_{L1}(\alpha_d). \tag{A.25}$$

A.5. Boeing–Vertol model

The Boeing–Vertol model (Tarzanin, 1972) assumes a relationship between the static and dynamic stall angle to determine a dynamic angle of attack α_d in the entire range of α. The relationship obtained by Gross and Harris (1969) is given as

$$\alpha_{ds} - \alpha_s = A_1 \sqrt{\frac{c|\dot{\alpha}|}{2V}}, \tag{A.26}$$

where α_{ds} is the dynamic stall angle as indicated in Fig. 16. Hence, the dynamic angle of attack should in some way be delayed with the right-hand side of Eq. (A.26) compared with the static angle of attack. This suggests setting

$$\alpha_d = \alpha - A_1 \sqrt{\frac{c|\dot{\alpha}|}{2V}} \frac{\dot{\alpha}}{|\dot{\alpha}|}, \tag{A.27}$$

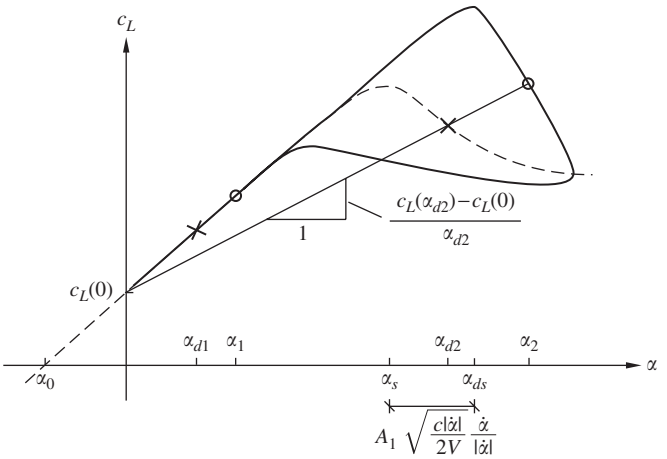

Fig. 16. Illustration of the Boeing–Vertol model. – –, Static lift. —, Dynamic lift. ×, Quasi-static angle of attack. ○, Dynamic angle of attack.

where a sign factor has been included in the delay term in order to consider both positive and negative values of $\dot\alpha$. Now $c_{L,d}$ is determined as

$$c_{L,d} = c_L(0) + \frac{c_L(\alpha_d) - c_L(0)}{\alpha_d}\alpha. \tag{A.28}$$

The theory of the model is illustrated in Fig. 16, where the static and dynamic lift curves are plotted as dashed and bold full lines, respectively. Consider an angle of attack α_1 in the linear domain during increasing α, hence $\dot\alpha>0$. Using Eq. (A.27) gives a related dynamic angle of attack α_{d1} which is less than α_1. Now, $c_L(\alpha_{d1})$ is evaluated indicated by (○), the slope of the line going from $c_L(\alpha_d)$ is evaluated, giving the fraction in Eq. (A.28). Finally, $c_{L,d}$ illustrated by (○) is determined from Eq. (A.28). In the linear domain, the slope determined at α_d is equal to the slope of the static lift, thus, no distinction can be made between the static and dynamic lift curve. Now, consider an angle of attack α_2 in the stall regime. Again, the corresponding dynamic angle of attack α_{d2} is found from Eq. (A.27). Then, the slope determined at α_d is less than that of the fully attached region, making $c_{L,d}(\alpha_2)$ less than that of a linear growing lift. This creates a dynamic stall cyclic behaviour as indicated in Fig. 16. For $\dot\alpha = 0$ it is easily seen that the combination of Eqs. (A.27) and (A.28) generates the static lift, i.e. the dynamic curve crosses the static curve for $\dot\alpha = 0$.

References

Abbott, I.H., von Doenhoff, A.E., 1959. Theory of Wing Sections. Dover Publications Inc., New York.

Akbari, M.H., Price, S.J., 2003. Simulation of dynamic stall for a NACA 0012 airfoil using a vortex method. Journal of Fluids and Structures 7, 855–874.

Bak, C., Madsen, H.A., Fuglsang, P., Rasmussen, F., 1999. Observations and hypothesis of double stall. Wind Energy 2, 195–210.

Beddoes, T.S., 1978. Onset of leading edge separation effects under dynamic conditions and low Mach numbers. In: Proceedings of the 34th Annual Forum of the American Helicopter Society.

Bisplinghoff, R.L., 1996. Aeroelasticity. Dover Publications Inc., New York.

Du, Z., Selig, M.S., 1998. A 3-D stall-delay model for horizontal axis wind turbine performance prediction. In: AIAA-98-0021, pp. 9–19.

Du, Z., Selig, M.S., 2000. The effect of rotation on the boundary layer of a wind turbine blade. Renewable Energy 20, 167–181.

Fung, Y.C., 1993. An Introduction to the Theory of Aeroelasticity. Dover Publications Inc., New York.

Green, R.B., Galbraith, R.A.M., Niven, A.J., 1992. Measurements of the dynamic stall vortex convection speed. Aeronautical Journal, 319–325.

Gross, D., Harris, F., 1969. Prediction of inflight stalled airloads from oscillating airfoil data. In: Proceedings of the 25th Annual National Forum of the American Helicopter Society.

Hansen, M.H., Gaunaa, M., Madsen, H.A., 2004. A Beddoes–Leishman type dynamic stall model in state-space and indicial formulations. Risø-R-1354(EN), Risø National Laboratory, Roskilde, Denmark.

Jones, R.T., 1940. The unsteady lift of a wing of finite aspect ratio. NACA Report 681, NACA.

Krenk, S., 2006. Airfoil theory for separated flow. Department of Mechanical Engineering, Technical University of Denmark, to be published.

Leishman, J.G., 1988. Validation of approximate indicial aerodynamic functions for two-dimensional subsonic flow. Journal of Aircraft 25, 917–922.

Leishman, J.G., 2000. Principles of Helicopter Aerodynamics. Cambridge University Press, Cambridge.

Leishman, J.G., Beddoes, T.S., 1986a. A semi-empirical model for dynamic stall. Journal of the American Helicopter Society 34, 3–17.

Leishman, J.G., Beddoes, T.S., 1986b. A generalised model for airfoil unsteady aerodynamic behaviour and dynamic stall using the indicial method. In: Proceedings of the 42nd Annual Forum of the American Helicopter Society.

Liiva, J., 1969. Unsteady aerodynamic and stall effects on helicopter rotor blade airfoil sections. Journal of Aircraft 6, 46–51.

Øye, S., 1991. Dynamic stall simulated as time lag of separation. Technical Report, Department of Fluid Mechanics, Technical University of Denmark.

Srinivasan, G.R., Ekaterinaris, J.A., McCroskey, W.J., 1995. Evaluation of turbulence models for unsteady flows of an oscillating airfoil. Computers and Structures 24, 833–861.

Suresh, S., Omkar, S.N., Mani, V., Prakash, T.N.G., 2003. Lift coefficient prediction at high angle of attack using recurrent neural network. Aerospace Science and Technology 7, 595–602.

Tarzanin, F.J., 1972. Prediction of control loads. Journal of the American Helicopter Society 17, 33–46.

Thwaites, B., 1960. Incompressible Aerodynamics. Clarendon Press, Oxford.

Tran, C.T., Petot, D., 1981. Semi-empirical model for the dynamic stall of airfoils in view of the application to the calculation of responses of a helicopter blade in forward flight. Vertica 5, 35–53.

VISCWIND, 1999. Viscous effects on wind turbine blades, final report on the JOR3-CT95-0007, Joule III project, Technical Report ET-AFM-9902, Technical University of Denmark.

Wernert, P., Geissler, W., Raffel, M., Kompenhans, J., 1996. Experimental and numerical investigations of dynamic stall on a pitching airfoil. AIAA Journal 34, 982–989.